Robotica (2016) volume 34, pp. 328–346. © Cambridge University Press 2014
doi:10.1017/S0263574714001441

Model development and boundary interaction force control of a piezoresistive-based microcantilever

Sohrab Eslami† and Nader Jalili‡*

†*Laboratory for Computational Sensing and Robotics, ERC—Computer Integrated Surgical Systems and Technology, Johns Hopkins University, Baltimore, MD 21218, USA*
‡*Piezoactive Systems Laboratory, Department of Mechanical and Industrial Engineering, Northeastern University, Boston, MA 02115, USA*

(Accepted May 12, 2014. First published online: June 13, 2014)

SUMMARY
Robots with micro- and nanoresolution of motion are becoming more practical and useful in many precision manufacturing processes and industries such as medical instruments and imaging tools. Apparently, the most important features of these devices are their precision and durability. As accuracy increases, more delicate tasks may be performed. Along this line, a spatial micromanipulator with three revolute–revolute–prismatic joints while equipped with nanometer motion resolution is considered here. At the end of the micromanipulator, a piezoresistive-based microcantilever operates as a force sensor to quantify the amount of the strain generated in the microcantilever and transduces it into a proper voltage for force sensing applications. In terms of the controller design, the value of the produced voltage can further be implemented as the feedback entering into the control loop and making the control unit to produce appropriate signals for manipulating the robot arm. A challenging and important problem is the need to control the applied boundary forces at the contact zone with external objects (specifically the biological samples). The ability to control the interaction force is of most interest today which has numerous applications in precision manufacturing and biomedical engineering. For this purpose, two types of controllers are presented here: a Lyapunov-based proportional-derivative (PD) controller and a robust adaptive (RA) controller. The performance and the stability of these two controllers are examined and discussed thoroughly in this paper so that it can be interpreted that the robust adaptive controller is robust under presence of uncertainties in force tracking control purposes.

KEYWORDS: Hybrid rigid-flexible micromanipulator; Piezoresistive microcantilever; Static/Dynamic boundary force control; Lyapunov-based PD and robust adaptive control.

1. Introduction

A new trend in nanopositioning and nanomanipulation subjects has been recently observed in the literature from the vast majority of papers and published reports. There are broad applications of nanomanipulation and force control in physics, chemistry, material sciences, and life sciences ranging from grasping and pulling/pushing DNA or genes to nanoscale imaging and piercing a cell's membrane to inject or extract fluid from the cell.[1,2]

One of the most acknowledged and long-running methods of nanomanipulation is the Atomic Force Microscope (AFM) technique. The principle of the nanomanipulator system adds a virtual-reality interface to an AFM as an apparatus which is useful for imaging as well as manipulating nanomaterials.[3] Pushing, cutting, picking, placing, and orienting are considered as some tasks of AFM. A three-dimensional (3D) path planning approach is carried out by taking into account the sample surface topography. The benefit of this method is that the tip of the manipulator is able to move across the surface without collision with the surface irregularities.[4]

* Corresponding author. E-mail: n.jalili@neu.edu

https://doi.org/10.1017/S0263574714001441 Published online by Cambridge University Press

One of the new achievements in the AFM-based nanomanipulation is autonomous manipulation of very small objects after performing the path planning.[5] In ref. [5], an efficient way for manipulating the 1D nanomaterials such as carbon nanotubes (CNTs) is proposed. Some other studies on the design and modeling of microrobots are established in refs. [6, 7], in which both dynamics and several controllers for tracking manipulator positioning are considered. One of the most attractive applications of micromanipulators is grasping nanoparticles in such a way they would not be damaged or squeezed while being manipulated or grasped. It is observed that the force or visual feedback is one way to lessen the risk of damaging the object. Implementing various advanced controllers can overcome unmodeled nonlinear structural dynamics.

Recently, some researchers have modeled the rigid-flexible micromanipulators for tremendous opportunities in microsurgery. However, to the best of authors' knowledge, there is a lack of research effort on the rigid-flexible micromanipulator. Hence, there is a need for performing more research on these types of systems because of their versatility and outstanding capabilities. In ref. [8], a two-link rigid-flexible manipulator with a moving payload mass at the macroscale is studied. The payload mass considered there is not fixed at the end of the manipulator and can move along the link in a prescribed manner. In another related work, when a rigid-flexible robot manipulator is working in a moving environment under conditions of winds or vibrations, the position or orientation of operation is consistently varying.[9] Fenili *et al.*[10] have studied the State-Dependent Riccati Equation (SDRE) for control solution of a two-link rigid-flexible robot manipulator assessing the nonlinear coupling equations.

In class of sensors, a force sensor may be utilized for sensing the interaction forces present in the coupling region between the probe's tip and the sample. Researchers in ref. [11] have presented a 2D piezoresistive force sensing cantilever for monitoring the lateral and vertical forces with a nano-Newton resolution having potential applications in microsurgery, micromanipulation of objects, and biological assays. In a similar manner, a piezoresistive sensor with high precision and fast response time up to 1 kHz was built and integrated with a microscope patch-clamp electronics.[12]

For a sophisticated system comprising of nonlinear terms, there are various uncertainties such as unmodeled dynamics, signal noise, and disturbances. Therefore, designing an appropriate controller could affect the performance and stability of the whole system. There are, however, numerous studies on developing advanced control paradigms for different systems[13–17] with appealing applications in microsurgery such as eye microsurgery, neurosurgery, and micro/nanomanipulation of miniature objects.

This paper undertakes the kinematics and dynamics modeling of a piezoelectrically driven micro/nanomanipulator. The micromanipulator, named here MM3A®,[1] has three degrees-of-freedom (DOF) with the respective revolute–revolute–prismatic (RRP) joints. The Nanomotor® implemented in MM3A® is composed of one slider and one stator (piezocrystal). By taking into account these characteristics, a 3-DOF model of this manipulator is studied. Furthermore, by utilizing the Denavit–Hartenberg convention, the transformation matrices are derived such that they would result in determining the position and orientation of the end effector. For deriving the equations of motion of the micromanipulator, the Euler–Lagrange formulation is applied by extracting the kinetic and potential energies as well as the virtual work. The piezoresistive microcantilever (PMC), as a force sensor plugged into the end of the micromanipulator, is sought to be modeled to relate the measured tip–sample interaction force to the output voltage. On the other hand, a linear tip–sample interaction force is considered to represent the effect of the applied force to the tip of the microcantilever. The produced voltage can further be used for the controller design purposes. The novelty of this work is considering a complex problem comprising a rigid (a spatial manipulator) and flexible (microcantilever) system such that the desired amount of the interaction force is used as a measure for determining the inputs to the micromanipulator's joints while other similar works only consider a flexible beam under an interaction force.

The dimension of the microcantilever is at least 50 times smaller than the size of the micromanipulator's links; thereby, by a good approximation those terms associated or multiplied by the microcantilever's geometrical dimension could be ignored. In the control development analysis, this type of unmodeled dynamics could be properly compensated by choosing an advanced controller. In the control scheme analysis, two types of controllers are studied: a Lyapunov-based PD controller which may be proper for the Static Boundary Force Control (SBFC) problem when there exists no dynamic force. In order to compensate for time-varying uncertainties in the system, the designed PD

https://doi.org/10.1017/S0263574714001441 Published online by Cambridge University Press

Table I. Denavit–Hartenberg convention.

i	α_{i-1}	a_{i-1}	d_i	θ_i
1	0	0	0	θ_1
2	90^0	L_1	0	θ_2
3	0	L_2	0	0
4	0	d	0	0

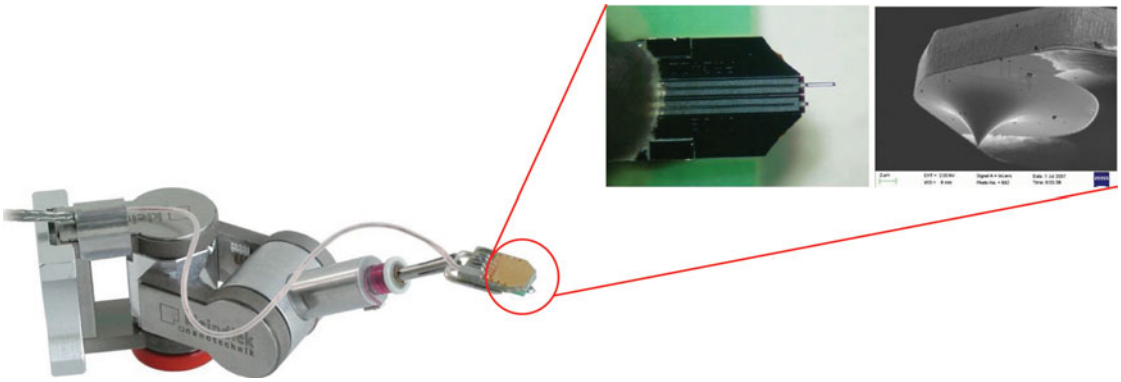


Fig. 1. MM3A® Micro/Nanomanipulator with the piezoresistive microcantilever (PMC) and its tip.[18]

controller may not be adequately robust to handle the dynamic force due to ever-present uncertainties. Hence, a robust adaptive (RA) controller is additionally targeted for the Dynamic Boundary Force Control (DBFC) problem and the results are carried out for both types of controllers. The simulation results are compared together by giving an evidence on an acceptable performance and stability of the controllers for both static and dynamic force cases.

2. Mathematical Modeling

2.1. Kinematic and dynamic equations

The MM3A® system evaluated here has a 3-DOF manipulator with RRP joints (see Fig. 1). There are two rotational motors with 10^{-7} rad (5 nm) resolution for the first one, 10^{-7} rad (3.5 nm) resolution for the second one, and one linear Nanomotor® with 0.25 nm resolution for the third joint. The operating ranges for the first two revolute joints are 240^0, and 12 mm for the third one. Having a compact design and a wide workspace within range approximately 100 cm^3 are among the attractive characteristics of the MM3A®. There exists no backlash or reverse shortfall in the joints during the motion which can be highlighted as one of most important properties of the MM3A®, in addition, it can operate with a high velocity up to 10 mm/s. The Nanomotor® implemented in MM3A® is composed of one slider and one stator (piezocrystal). When the slider rotates, by touching the stator it holds the stator by friction in place. By application of an electrical voltage, the stator can expand or contract; therefore, the Nanomotor® is able to move in two different modes; namely, fine and coarse modes.[1]

MM3A® can be mathematically substituted by a 3-DOF manipulator with RRP joints possessing a fixed base (see Fig. 1). This manipulator is able to manipulate in a 3D space such that the end effector is able to follow a determined path for some specific applications such as manipulating nanoparticles. Figure 1 shows an image of the MM3A® with a magnification on the PMC and its tip. The piezoresistive layer mounted on the microcantilever casting as a force sensing is to enable the system for measuring the mechanical forces at the micro/nanoscale.

Having a proper coordinate and using the Denavit–Hartenberg convention (see Table I) as well as the transformation matrix T in (1), the general transformation matrices are obtained.[19] By multiplying these transformations, a final transformation matrix which transforms the first coordinate to the last coordinate may be computed as given in (1). A 3D schematic drawing of this manipulator is shown

https://doi.org/10.1017/S0263574714001441 Published online by Cambridge University Press

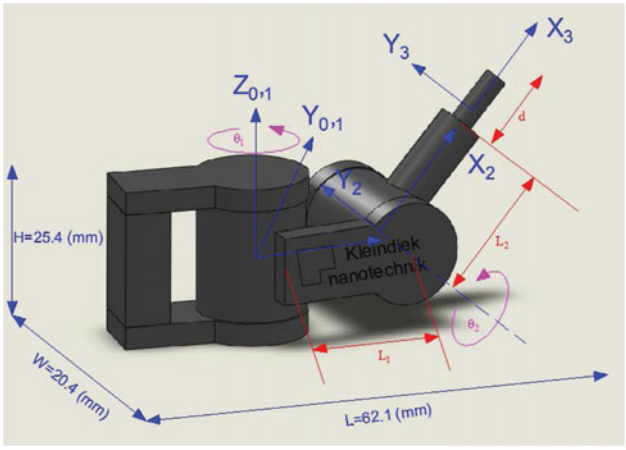


Fig. 2. A schematic view of the RRP spatial micromanipulator, MM3A®.

in Fig. 2. The first joint is a spatial one implying that this revolute joint could rotate about its vertical axis. The second revolute joint is always perpendicular to the rotation axis of the first joint while in motion. The third joint is a prismatic joint; hence, any spatial workspace can be created by this type of the RRP micromanipulator. Consequently, the appropriate coordinate system results in describing the position and orientation of the system as depicted in Fig. 2.

The kinematic parameters of the micromanipulator are shown in Table I, with the general form of the transformation matrix as given in (1):

$$ {}^{i-1}_{i}T = \begin{bmatrix} c\theta_i & -s\theta_i & 0 & a_{i-1} \\ s\theta_i c\alpha_{i-1} & c\theta_i c\alpha_{i-1} & -s\alpha_{i-1} & -s\alpha_{i-1}d_i \\ s\theta_i s\alpha_{i-1} & c\theta_i s\alpha_{i-1} & c\alpha_{i-1} & c\alpha_{i-1}d_i \\ 0 & 0 & 0 & 1 \end{bmatrix}, \tag{1} $$

where c and s denote the cosine and sine and i is corresponding to the number of each proper link, respectively.

By computing the kinematics equations, the position of the micromanipulator's end effector may be obtained as:

$$ \begin{bmatrix} P_x \\ P_y \\ P_z \end{bmatrix} = \begin{bmatrix} c_1(L_1 + L_2c_2 + dc_2) \\ s_1(L_1 + L_2c_2 + dc_2) \\ s_2(L_2 + d) \end{bmatrix}, \tag{2} $$

where P_x, P_y, and P_z are the positions of the end effector in three principal directions, respectively.

Considering a frame illustrated in Fig. 3, the position vector of three links, microcantilever ($\vec{r}_{MC}$), and the tip mass ($\vec{r}_{me}$) are described as follows:

$$ \vec{r}_1 = \frac{L_1}{2}c_1\hat{i} + \frac{L_1}{2}s_1\hat{j}, \tag{3} $$

$$ \vec{r}_2 = \left[L_1 + \frac{L_2}{2}c_2\right]c_1\hat{i} + \left[L_1 + \frac{L_2}{2}c_2\right]s_1\hat{j} + \frac{L_2}{2}s_2\hat{k}, \tag{4} $$

$$ \vec{r}_3 = \left[L_1 + L_2c_2 + \frac{d(t)}{2}c_2\right]c_1\hat{i} + \left[L_1 + L_2c_2 + \frac{d(t)}{2}c_2\right]s_1\hat{j} + \left[L_2 + \frac{d(t)}{2}\right]s_2\hat{k}, \tag{5} $$

https://doi.org/10.1017/S0263574714001441 Published online by Cambridge University Press

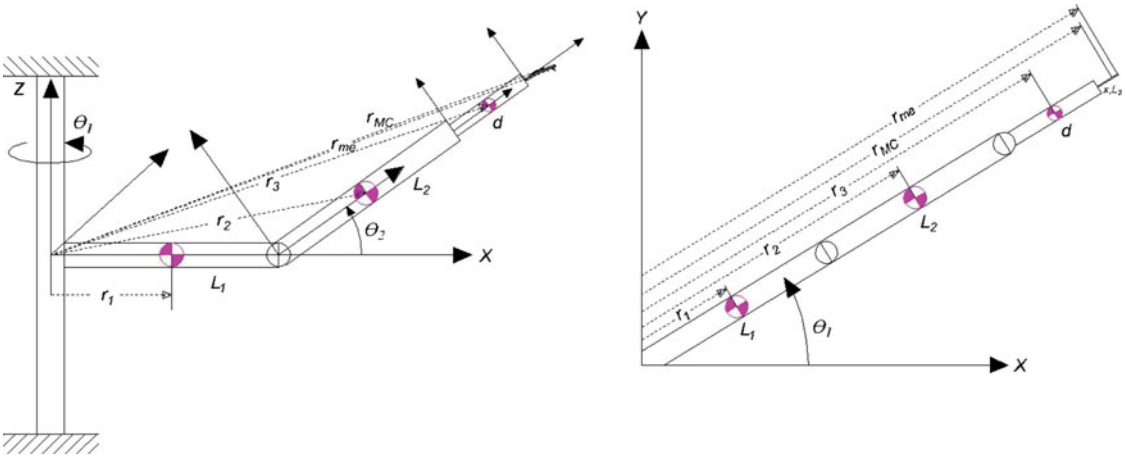


Fig. 3. XZ (side) and XY (top) views of the 3-DOF RRP micromanipulator with the PMC.

$$\vec{r}_{MC} = [L_1 + L_2c_2 + (d(t) + x)c_2 + w(x,t)s_2]\, c_1\hat{i} + [L_1 + L_2c_2 + (d(t) + x)c_2 + w(x,t)s_2]\, s_1\hat{j} + [L_2 + (d(t) + x)s_2 - w(x,t)c_2]\,\hat{k}, \tag{6}$$

$$\vec{r}_{m_e} = [L_1 + L_2c_2 + (d(t) + L_3)c_2 + w(L_3,t)s_2]\, c_1\hat{i} + [L_1 + L_2c_2 + (d(t) + L_3)c_2 + w(L_3,t)s_2]s_1\hat{j} + [L_2 + (d(t) + L_3)s_2 - w(L_3,t)c_2]\, s_2\hat{k}, \tag{7}$$

where $L_1, L_2,$ and $d(t)$ are the length of the three rigid links (see Figs. 2 and 3), $w(x,t)$ is the microcantilever's transverse displacement from its neutral axis, and L_3 is the length of the microcantilever.

In order to find the equations of motion for the rigid-flexible micromanipulator described here, the kinetic and potential energies as well as the virtual work are extracted for plugging into the extended Hamilton's principle in the following manner. For this end, the kinetic energy of the system can be given as:

$$T = \frac{1}{2}m_1V_{G_1}^2 + \frac{1}{2}I_{CG_1}{}^1\omega_1^2 + \frac{1}{2}m_2V_{G_2}^2 + \frac{1}{2}I_{CG_2}{}^2\omega_2^2 + \frac{1}{2}m_3V_{G_3}^2 + \frac{1}{2}I_{CG_3}{}^3\omega_3^2 + \frac{1}{2}m_e\dot{r}_{me}^2 + \frac{1}{2}\int_0^{L_3}\rho(x)A\dot{r}_{MC}^2dx, \tag{8}$$

where $\vec{V}_{G_1} = \dot{\vec{r}}_1$, $\vec{V}_{G_2} = \dot{\vec{r}}_2$, $\vec{V}_{G_3} = \dot{\vec{r}}_3$, and $m_1, m_2, m_3,$ and m_e are the masses of three rigid links and microcantilever's tip mass, respectively. I_{CG_i} is the moment of inertia for the corresponding link and ${}^i\omega_i$ is the angular velocity of the corresponding link with $i = 1, 2, 3$, A is the cross-sectional area of the microcantilever, and $\rho(x)$ is the volumetric density defined as:

$$\rho(x) = (S(x)\rho_p t_p + \rho_b t_b)b, \tag{9}$$

where ρ_p is the piezoresistive layer volumetric density and b is the width of the microcantilever which is equal to the width of the piezoresistive layer (b_p), and t_b and t_p are the thicknesses of the microcantilever and piezoresistive layers, respectively.[20]

In (9), function $S(x)$ is defined as:

$$S(x) = H(x - x_1) - H(x - x_2), \tag{10}$$

https://doi.org/10.1017/S0263574714001441 Published online by Cambridge University Press

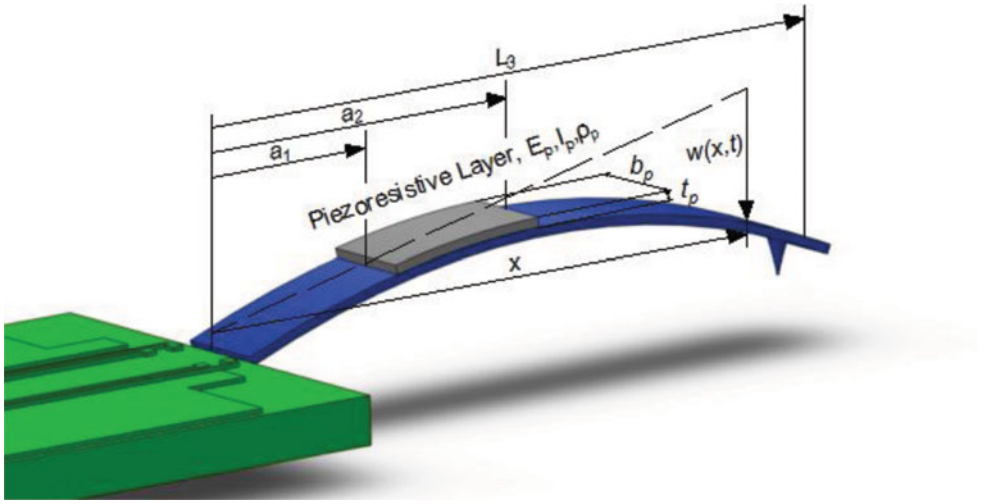


Fig. 4. A schematic drawing of the PMC.

where $H(x)$ is the Heaviside function (a unit step function) and is defined as:

$$H(x - x_i) = \begin{cases} 0 & \text{for } x < x_i, \\ 1 & \text{for } x \geq x_i. \end{cases} \quad i = 1, 2 \tag{11}$$

The potential energy can also be expressed as:

$$U = m_2 g \frac{L_2}{2}(1 - s_2) + m_3 g \left(L_2 + \frac{d}{2}\right)(1 - s_2) + \frac{1}{2}\int_0^{L_3} EI(x)(w''(x,t))^2 dx \tag{12}$$

where

$$EI(x) = E_b I_b + E_p I_p S(x), \tag{13}$$

$$E_b I_b = \frac{1}{12} b E_b t_b^3, \quad \text{and } E_p I_p = b E_p t_p \left[\frac{t_b^2}{4} + \frac{t_b t_p}{2} + \frac{t_p^2}{3} - \frac{z_n}{2}(t_b + t_p)\right] \quad \text{for } z_n = \frac{E_p t_p (t_b + t_p)}{(E_b t_b + E_p t_p)}, \tag{14}$$

where $E_b I_b$ and $E_p I_p$ are the rigidity, E_b and E_p are the stiffness of the microcantilever and piezoresistive layer, respectively, and z_n is the neutral surface[20] in which all the parameters are presented in Fig. 4.

It should be noted here that the effect of the gravitational effect of the tip mass has been neglected due to its ultrasmall value when compared to the weight of the micromanipulator.

The nonconservative virtual work due to external loading and damping forces can be given as:

$$\delta W^{nc} = \tau_1(t)\delta\theta_1(t) + \tau_2(t)\delta\theta_2(t) + F(t)\delta d(t) + f_{ID}(t)\delta w(L_3, t) - B\int_0^{L_3} \dot{w}(x,t)\delta w(x,t)dx$$
$$- C\int_0^{L_3} \dot{w}'(x,t)\delta w(x,t)dx, \tag{15}$$

where τ_1, τ_2, F, and f_{ID} stand for the first and second joint torques, the joint force and atomic interaction force, respectively, and B and C are the respective viscous and structural damping coefficients.

https://doi.org/10.1017/S0263574714001441 Published online by Cambridge University Press

The extended Hamilton's principle is written as:

$$\int_{t_1}^{t_2} (\delta T - \delta U + \delta W^{nc}) dt = 0. \tag{16}$$

Using Eqs. (8)–(15) and substituting them into Eq. (16), integrating by parts, and after performing some manipulations and arrangements, it results in the general form of the robot manipulator dynamics as:[14,16]

$$M(q)\ddot{q} + V(q, \dot{q}) + (F_v\dot{q} + F_d) + G(q) + \tau_d = \tau \tag{17}$$

where $q(t) \in R^n$, $M(q)$ is the $n \times n$ inertia matrix, $V(q, \dot{q})$ is an $n \times 1$ Coriolis/centrifugal vector, F_v is the coefficient matrix of viscous friction, F_d is the dynamic friction, τ_d is the disturbance (e.g., parameter uncertainties), $G(q)$ is an $n \times 1$ gravity vector, and $\tau(t)$ is an $n \times 1$ control input.

After applying Eqs. (3)–(7) into Eqs. (8) and (12), four nonlinear equations of motion for the hybrid rigid-flexible micromanipulator and microcantilever can be obtained. In such a procedure, those terms with similar coefficients must be set equal to zero; hence, the system of nonlinear partial differential equations (PDEs) representing the micromanipulator's dynamics along with the microcantilever's nonlinear PDE as the flexible structure may be attained. One of the main advantages of this technique is obtaining the boundary condition (BC) equations directly as the result of this approach. Equation (18) associated with 4 BCs of the microcantilever is followed by:

$$\begin{aligned}
w(0, t) &= 0, \\
w'(0, t) &= 0, \\
w''(L_3, t) &= 0, \\
-m_e(\ddot{\theta}_2(t)(L_3 + L_2 + d(t)) + 2\dot{\theta}_2(t)\dot{d}(t) - \ddot{w}(L_3, t) + \dot{\theta}_1^2(t)L_1 s_2 - \dot{\theta}_1^2(t)w(L_3, t)c_2^2 \\
+ \dot{\theta}_1^2(t)(L_3 s_2 c_2 + L_2 s_2 c_2 + d(t)s_2 c_2) + w(L_3, t)(\dot{\theta}_1^2(t) + \dot{\theta}_2^2(t))) + EI(x)w'''(L_3, t) = f_{ID}(t).
\end{aligned} \tag{18}$$

It is evident that Eq. (18) forms the nonhomogenous BCs due to the harmonic excitation and the existence of the interaction force and needs to be homogenized by applying the following change of variable:

$$w(x, t) = z(x, t) + f_{ID}(t)g_1(x) + h_1(t)g_2(x) + h_2(t)g_3(x), \tag{19}$$

where $g_1(x)$, $g_2(x)$, and $g_3(x)$ are some geometrical functions for $0 \le x \le L_3$ achieved by forcing the BCs to be homogeneous based on the new variable $z(x, t)$. The nonlinear terms $h_1(t)$ and $h_2(t)$ as well as geometrical functions $g_1(x)$, $g_2(x)$, and $g_3(x)$ can be acquired as follows:

$$\begin{aligned}
h_1(t) &= \ddot{\theta}_2(t)(L_3 + L_2 + d(t)) + 2\dot{\theta}_2(t)\dot{d}(t) + \dot{\theta}_1^2(t)L_1 s_2 \\
&\quad + \dot{\theta}_1^2(t)(L_3 s_2 c_2 + L_2 s_2 c_2 + d(t)s_2 c_2),
\end{aligned} \tag{20}$$

$$h_2(t) = -\dot{\theta}_1^2(t)w(L_3, t)c_2^2 + w(L_3, t)(\dot{\theta}_1^2(t) + \dot{\theta}_2^2(t)), \tag{21}$$

$$g_1(0) = 0, \quad g_1'(0) = 0, \quad g_1''(L_3) = 0, \quad g_1(L_3) = 0, \quad g_1'''(L_3) = -\frac{1}{EI(x)}, \tag{22}$$

$$g_1(x) = -\frac{1}{18EI(x)L_3}\left(2x^4 - 5L_3x^3 + 3L_3^2x^2\right), \tag{23}$$

$$g_2(x) = x^3(1 - L_3), \quad g_3(x) = -\frac{1}{2}x^3(1 - L_3). \tag{24}$$

We use the assumed mode model (AMM) expansion to truncate the PDE of the microcantilever for the purpose of the numerical simulations since there is no analytical solution to the aforementioned

https://doi.org/10.1017/S0263574714001441 Published online by Cambridge University Press

equation ((17) along with BCs (18)):

$$w(x,t) = \sum_{i=1}^{N} \varphi_i(x) w_i(t), \tag{25}$$

where $\varphi_i(x)$ is a set of admissible functions to satisfy the BCs of a microcantilever with a tip mass at the end[21,22] and $w_i(t)$ denotes the generalized coordinates.

Different models are studied for the tip–sample interaction,[21] but in the simulation environment and in order to simply correlate the voltage produced by the piezoresistive layer and the interaction force, $f_{ID}(t)$, the following simple model is used:[23]

$$f_{ID}(t) = \frac{E^b b t_b}{4L_3^3} w(L_3, t). \tag{26}$$

According to Eq. (25), $w(L_3, t)$ in which N denotes the number of vibration modes can be expanded as:

$$w(L_3,t) = \varphi_1(L_3)w_1(t) + \varphi_2(L_3)w_2(t) + \ldots + \varphi_i(L_3)w_i(t). \tag{27}$$

Relation (26) implies that the interaction force $f_{ID}(t)$ is a function of the microcantilever's transverse displacement ($\sum_{i=1}^{N} \varphi_i(L_3)w_i(t)$, for L_3 being the microcantilever's length) and can be implemented on the proposed model for the microcantilever.

2.2. Piezoresistive modeling preliminaries

Kleindiek® Nanotechnik Co. provides various plug-in-tools for different applications as one of them is the force sensor (http://www.nanotechnik.com/mgs2-em.html). There are two types of force sensors depending on the precision purposes: FMT-400 and FMT-120 sensors. The compact force readout FMT-400 model (used in this research) has lower force sensing capability up to 80 μN comparing to FMT-120 model which can feel up to 360 μN. Tip force constant of FMT-400 is 2–4 (N/m) and 500–650 Ω is the range of the resistance with sensitivity of 3.1×10^{-3}mV/nm. The voltage of 2.5 V is applied to all types of the force sensors.

By taking into account the features of the PMC sensor, the change of the resistance of this layer and the output voltage from the Wheatstone bridge, V_0, may be related as:[24]

$$V_0 = \frac{1}{4}\frac{\Delta R}{R} V_s, \tag{28}$$

where $\frac{\Delta R}{R}$ is the relative resistance change and V_s is the supply voltage. ΔR in (28) can be obtained as:[25]

$$\Delta R = \frac{\partial R}{\partial L_p}\Delta L_p - \frac{\partial R}{\partial b_p}\Delta b_p + \frac{\partial R}{\partial \rho_p}\Delta \rho_p, \tag{29}$$

where L_p, b_p, and ρ_p are respective length, width, and the resistivity of the piezoresistive layer. However, the values for ΔL_p, Δb_p, and $\Delta \rho_p$can be calculated in the following form:[24]

$$\Delta L_p = L_p \varepsilon_x, \tag{30}$$

$$\Delta b_p = b_p \varepsilon_y, \tag{31}$$

$$\Delta \rho_p = \rho_p \frac{E(\pi_x + \nu\pi_y)\varepsilon_x + E(\pi_y + \nu\pi_x)\varepsilon_y}{1-\nu^2}, \tag{32}$$

https://doi.org/10.1017/S0263574714001441 Published online by Cambridge University Press

where π_x and π_y are the longitudinal and transverse piezoresistive coefficients, respectively, and ν is the Poisson ratio of the piezoresistive layer. The longitudinal strain can be expressed as:[20,26]

$$\varepsilon_x = \begin{cases} -z\dfrac{\partial^2 w(x,t)}{\partial x^2} & \text{if } x < a_1 \text{ or } x > a_2, \\ -(z-z_n)\dfrac{\partial^2 w(x,t)}{\partial x^2} & \text{if } a_1 < x < a_2, \end{cases} \tag{33}$$

where z_n is the neutral surface and defined in Eq.(14).

Utilizing Eqs. (28)–(32) and substituting into Eq. (29), it yields:

$$\begin{aligned} \Delta R = &-\frac{\partial R}{\partial L_p} L_p (z-z_n) \int_{a_1}^{a_2} \frac{\partial^2 w(x,t)}{\partial x^2} dx - \frac{\partial R}{\partial b_p} b_p (z-z_n) \int_{a_1}^{a_2} \frac{\partial^2 w(x,t)}{\partial x^2} dx \\ &- \frac{\partial R}{\partial \rho_p} \rho_p \frac{E(\pi_x + \nu\pi_y)\varepsilon_x + E(\pi_y + \nu\pi_x)\varepsilon_y}{1-\nu^2} (z-z_n) \int_{a_1}^{a_2} \frac{\partial^2 w(x,t)}{\partial x^2} dx \end{aligned} \tag{34}$$

$$\begin{aligned} \Delta R = &-\frac{\partial R}{\partial L_p} L_p (z-z_n) \left. \frac{\partial w(x,t)}{\partial x} \right|_{a_1}^{a_2} - \frac{\partial R}{\partial b_p} b_p (z-z_n) \left. \frac{\partial w(x,t)}{\partial x} \right|_{a_1}^{a_2} \\ &- \frac{\partial R}{\partial \rho_p} \rho_p \frac{E(\pi_x + \nu\pi_y)\varepsilon_x + E(\pi_y + \nu\pi_x)\varepsilon_y}{1-\nu^2} (z-z_n) \left. \frac{\partial w(x,t)}{\partial x} \right|_{a_1}^{a_2} \end{aligned} \tag{35}$$

Employing Eqs. (19) and (25), Eq. (35) can be rearranged as:

$$\begin{aligned} \Delta R = &-\frac{\partial R}{\partial L_p} L_p (z-z_n) \left(\varphi_i'(x) w_i(t) + f_{ID}(t) g_1(x) + h_1(t) g_2(x) + h_2(t) g_3(x)\right)\Big|_{a_1}^{a_2} \\ &- \frac{\partial R}{\partial b_p} b_p (z-z_n) \left(\varphi_i'(x) w_i(t) + f_{ID}(t) g_1(x) + h_1(t) g_2(x) + h_2(t) g_3(x)\right)\Big|_{a_1}^{a_2} \\ &- \frac{\partial R}{\partial \rho_p} \rho_p \frac{E(\pi_x + \nu\pi_y)\varepsilon_x + E(\pi_y + \nu\pi_x)\varepsilon_y}{1-\nu^2} (z-z_n)(\varphi_i'(x) w_i(t) + f_{ID}(t) g_1(x) \\ &+ h_1(t) g_2(x) + h_2(t) g_3(x))\Big|_{a_1}^{a_2} \end{aligned} \tag{36}$$

After finding the values for ΔR and substituting them into Eq. (28) and using Eq. (36), it is now obvious that V_0 and f_{ID} are related and can be correlated through the process described here. It results in an implicit relation where $f_{ID}(t)$ and $w_i(t)$ are dependent on each other and it can be resolved by setting an initial condition on $w_i(t)$ or $\dot{w}_i(t)$ (as the initial displacement or the initial velocity).

3. Control Development

In this section, for the purpose of acquisition of the desired force, two types of controllers are investigated: a Lyapunov-based PD controller and a robust adaptive controller for a rigid-flexible micromanipulator with the associated microcantilever.

3.1. Lyapunov-based PD controller

For the aim of control design, first, a linear controller is studied that works for the manipulator described in the previous section. Adopting a one-dimensional general interaction force as represented in Eq. (26), our goal is to let $f_{ID}(t)$ approach the desired interaction force $f_{ID}^D(t)$ when applying an appropriate torque to the second revolute joint and force to the third prismatic joint to form a configuration for the manipulator to move in the vertical direction. Therefore, the error signals can be defined as follows:

$$e_1(t) = \theta_2(t) - \theta_2^D(t), \tag{37}$$

$$e_2(t) = d(t) - d^D(t), \tag{38}$$

https://doi.org/10.1017/S0263574714001441 Published online by Cambridge University Press

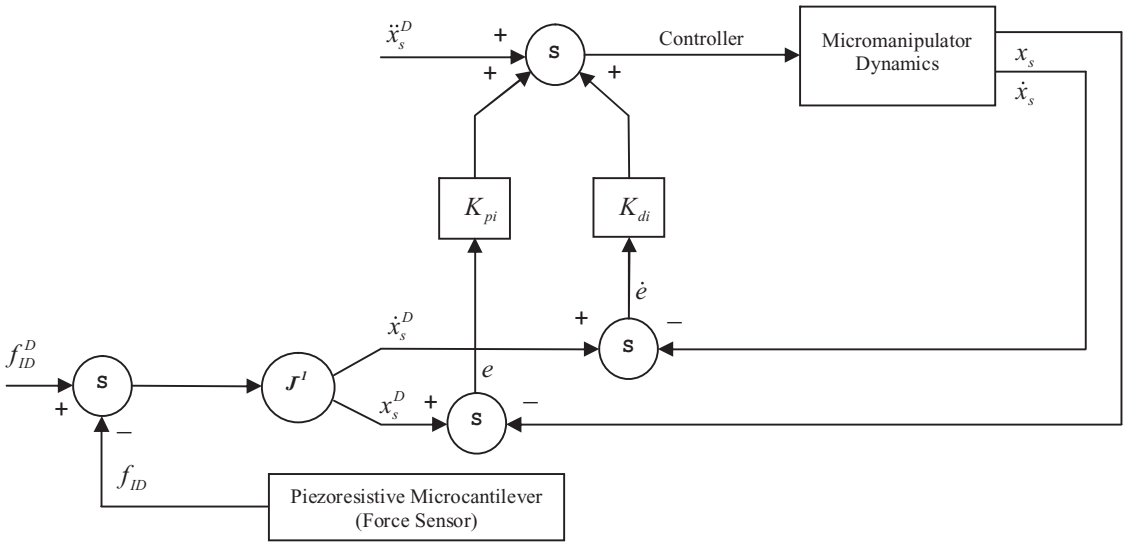


Fig. 5. PD controller block diagram.

$$e_3(t) = f_{ID}(t) - f_{ID}^D(t). \tag{39}$$

Since $\theta_1(t)$ has a motion in the 3D space, at this point, there may not be a need for designing a controller to track the one-dimensional boundary force in the vertical direction. In this study, the intention of the piezoresistive microcantilever assumption is sensing the interaction force. Therefore, based on the amount of the produced voltage in the piezoresistive layer the controller is able to make a proper decision on how much and in which "direction" the micromanipulator should move to control the interaction force. The "direction" here means the vertical motion (up or down only) which can be generated by the proper combination of the second revolute and third prismatic joints.

In Eq. (2) by having $\ddot{P}_x$, $\ddot{P}_y$, $\ddot{P}_z$ parameters and $\theta_2^D(t)$ and $d^D(t)$ (as the desired values of the system's state variables), the dynamic equations of the micromanipulator and piezoresistive microcantilever could be solved simultaneously.

The following is the structure of the proposed Lyapunov-based PD controller:

$$\tau_1(t) = -K_{p1}e_1(t) - K_{d1}\dot{e}_1(t), \tag{40}$$

$$F(t) = -K_{p2}e_2(t) - K_{d2}\dot{e}_2(t), \tag{41}$$

where K_{p1}, K_{p2}, K_{d1}, and K_{d2} are some positive control gains that must be adjusted during the simulation. Figure 5 depicts a block diagram of the proposed PD controller in which x_s stands for the state variables $\theta_1, \theta_2, d, w(L_3, t)$.

By taking into account the total energy of the system, a candidate Lyapunov function can be chosen as:

$$\begin{aligned} V_1(t) = {} & \frac{1}{2}m_1V_{G_1}^2 + \frac{1}{2}I_{CG_1}{}^1\omega_1^2 + \frac{1}{2}m_2V_{G_2}^2 + \frac{1}{2}I_{CG_2}{}^2\omega_2^2 + \frac{1}{2}m_3V_{G_3}^2 + \frac{1}{2}I_{CG_3}{}^3\omega_3^2 + \frac{1}{2}m_e\dot{r}_{me}^2 \\ & + \frac{1}{2}\int_0^{L_3}\rho(x)A\dot{r}_{MC}^2dx + m_2g\frac{L_2}{2}(1-s_2) + m_3g\left(L_2 + \frac{d}{2}\right)(1-s_2) \\ & + \frac{1}{2}\int_0^{L_3}EI(x)(w''(x,t))^2dx + \frac{1}{2}K_{p1}e_1^2 + \frac{1}{2}K_{p2}e_2^2. \end{aligned} \tag{42}$$

By taking the time derivative of the Lyapunov function (42) with respect to time, replacing equations of motion, performing some manipulations, arrangements, and omitting the centrifugal terms, and

https://doi.org/10.1017/S0263574714001441 Published online by Cambridge University Press

taking account of it into (40), it results in:

$$\dot{V}_1(t) = \dot{\theta}_1 K_{d1} \dot{e}_1 + \dot{d} K_{d2} \dot{e}_2, \tag{43}$$

and when $\dot{\theta}_1^D(t)$, $\dot{\theta}_2^D(t)$, and $\dot{d}^D(t)$ set to zero, (43) reduces to:

$$\dot{V}_1(t) = -K_{d1} \dot{\theta}_1^2 - K_{d2} \dot{d}^2. \tag{44}$$

For some constant positive values of K_{d1} and K_{d2}, it can be concluded that:

$$\dot{V}_1(t) \leq 0. \tag{45}$$

Due to the positive semidefiniteness nature of (42) and negative semidefiniteness nature of Eq. (45), all signals $V_{G_1}, V_{G_2}, V_{G_3}, {}^1\omega_1, {}^2\omega_2, {}^3\omega_3, \dot{r}_{me}, \dot{r}_{MC}, w(x,t) \in L_\infty$. The asymptotic stability of the system can be concluded by applying the LaSalle's theorem to yield $\lim_{t\to\infty} e(t) = 0$.

Equations (40) and (41) are the control inputs that must be applied to the second and third links to manipulate the robot arm. For real applications, due to the unmodeled dynamics of the system, external disturbances, signal noises and generally any different types of uncertainties, this form of linear controller may not be able to compensate those factors. Hence, an advanced controller scheme is required.

3.2. Robust adaptive controller

A need for the advanced controller under different types of uncertainties, unmodeled dynamics, noises, and sensor nonlinear mismatch is felt; therefore, a robust adaptive controller is demanded for the hybrid rigid-flexible piezoresistive-based micromanipulator problem as developed in this section.

Considering (17), the error vector can be defined as a combination of the error signal and its time derivative as:

$$e = \begin{bmatrix} e \\ \dot{e} \end{bmatrix}, \tag{46}$$

where e was earlier defined in Eqs. (37)–(39).

Because of various types of uncertainties present in the system, a positive function $\eta \in \mathbb{R}^1$ may be used as upper and lower bounds of uncertainties as:[14–16]

$$\left\| M(q)(\ddot{q}^D + \dot{e}) + V(q,\dot{q})(\dot{q}^D + e) + G(q) \right\| \leq \eta, \tag{47}$$

where $q^D(t) \in \mathbb{R}^1$ is the desired value of the state variable already expressed in Eqs. (37)–(39) for each individual term (i.e., θ_2, d, f_{ID}). η is defined in the following form:

$$\eta = \gamma_0 + \gamma_1 \|e\| + \gamma_2 \|e\|^2 \geq \left\| M(q)(\ddot{q}^D + \dot{e}) + V(q,\dot{q})(\dot{q}^D + e) + G(q) \right\|, \tag{48}$$

where γ_0, γ_1 and γ_2 are the constant positive values that are chosen based on uncertainties, disturbances, noises, tip mass, etc.[13,14]

The proposed robust adaptive controller can be formulated as:

$$u = K_u r + \frac{r\hat{\eta}^2}{\beta + \hat{\eta}\|r\|}, \tag{49}$$

where K_u is a $n \times n$ diagonal and positive-definite matrix, $\beta \in \mathbb{R}^1$ a positive control constant, and r is the filtered tracking error defined as:[13–15]

$$r = e + \dot{e} \tag{50}$$

https://doi.org/10.1017/S0263574714001441 Published online by Cambridge University Press

3.2.1. Stability analysis. After designing the controller, it is essential to consider its stability; therefore, intuitively a Lyapunov candidate function can be selected as:[14,16]

$$V_2 = \frac{1}{2}\delta^{-1}\,\tilde{\Theta}^2 + \frac{1}{2}M(q)r^2 + K_c\beta, \tag{51}$$

where $\hat{\Theta}$ a 3×1 unknown parameters vector $\hat{\Theta} = [\,\hat{\gamma}_0\ \hat{\gamma}_1\ \hat{\gamma}_2\,]^T$, and $K_c$is a positive control gain given by:

$$K_c = -\frac{\beta}{\dot{\beta}} \quad \beta(0) > 0. \tag{52}$$

And the adaptive law as:

$$\dot{\hat{\Theta}} = -\delta\,\Xi^T\,\|r\|\,, \tag{53}$$

where the 1×3 regression matrix Ξ is defined as:

$$\Xi = \left[\,1\ \|e\|\ \|e\|^2\,\right]. \tag{54}$$

Taking time derivative of Eq.(51) and performing some mathematical manipulation, it could lead us to:

$$\dot{V}_2 \leq -r^T K_u r + K_c\dot{\beta} + \frac{\beta\,\Xi\hat{\Theta}\,\|r\|}{\Xi\hat{\Theta}\,\|r\| + \beta} \leq 0. \tag{55}$$

Inequality (55) holds since the last two terms (for $K_c\dot{\beta} = -\beta < 0$) are always less than zero and accordingly $\dot{V}_2$ is bounded by:

$$\dot{V}_2 \leq -r^T K_u r. \tag{56}$$

Since the Lyapunov function chosen here is positive semidefinite and its time derivative is negative semidefinite; consequently, it results in the boundedness properties of signals $\dot{r}(t)$, $r(t)$, $\dot{e}(t)$ and $e(t) \in L_\infty$; hence, by using the Barbala's lemma,[13,27] it can be concluded that:

$$\lim_{t\to\infty} e(t) = 0 \tag{57}$$

This concludes the asymptotically stability situation for the position tracking error signal of the designed robust adaptive controller.[13–15]

4. Simulation Results and Discussions

To assess the performance and stability characteristics of the controllers designed in the preceding section, a numerical example is considered along with an extensive comparative study.

The simulation results of the PD and the robust adaptive controllers are presented in this section and their performances are discussed together. Referring to Fig. 2, for sensing the boundary interaction force, the MM3A® needs to make a proper movement such that the second joint moves around its rotation axis; thereby the MM3A®'s end effector moves the tip in the vertical direction. Since the interaction force studied here has only one direction along the Z_0 axis, there is no need to assume that the first joint's movement is restricted to the horizontal plane; therefore, the first joint can be presumed fixed having no motion. Such assumption may not limit any derivations of the controller design. For more advanced cases, considering the other directions of the interaction force, such as the friction force microscopy (FFM) technique, the rotation of the first joint is indeed required to affect the boundary interaction force. Table II lists the numerical values of the micromanipulator as well as the piezoresistive microcantilever force sensor for the purpose of simulation.

Tables III and IV list the Lyapunov-based PD and the robust adaptive controller parameters and gains. The controller gains obtained in Tables III and IV are based on reducing the error signals

https://doi.org/10.1017/S0263574714001441 Published online by Cambridge University Press

Table II. Piezoresistive microcantilever modeling preliminaries.

Symbol	Properties	Value (Unit SI)
L_1	Micromanipulator first link length	2105×10^{-5} m
L_2	Micromanipulator second link length	1737×10^{-5} m
d	Micromanipulator third link length	500×10^{-5} m
m_1	Mass of the first link	20000×10^{-6} Kg
m_2	Mass of the second link	20000×10^{-6} Kg
m_3	Mass of the third link	5000×10^{-6} Kg
m_e	Mass of the tip mass	5.27×10^{-13} Kg
I_{CG_1}	Moment of inertia (first link)	0.1040 m^4
I_{CG_2}	Moment of inertia (second link)	0.1225 m^4
I_{CG_3}	Moment of inertia (third link)	0.1000 m^4
E_b	Microcantilever Young modulus	150×10^9 Pa
L_3	Microcantilever beam length	393×10^{-6} m
b	Microcantilever beam width	25×10^{-6} m
t_b	Microcantilever beam thickness	1×10^{-6} m
ρ	Microcantilever beam density	2330 Kg/m^3
E_p	Piezoresistive Young modulus	160×10^9 Pa
$L_p = a_2 - a_1$	Piezoresistive layer length	25×10^{-6} m
ρ_p	Piezoresistive beam density	7750 Kg/m^3
C	Microcantilever structural damping	0.01 Kg/s

Table III. Controller gains of the Lyapunov-based PD controller.

Symbol	Properties	Value (Unit SI)
K_{p1}	Controller gain	1100
K_{p2}	Controller gain	2300
K_{d1}	Controller gain	42
K_{d2}	Controller gain	53

Table IV. Controller gains of the robust adaptive Controller.

Symbol	Properties	Value (Unit SI)
K_c	Controller gain	1
K_u	Controller gain	88
δ	Controller gain	10
η	Controller gain	20

defined in Eqs. (37)–(39) and achieving an acceptable performance of the controller which is tracking the desired interaction force herein.

The designed Lyapunov-based PD controller may be routine for controlling this type of problem but lack of capability to compensate for the conditions under presence of uncertainties and disturbances in the real system makes it inaccurate for real experiments.

In the case of SBFC, here, a step input is applied to the system when the desired state is only approaching a desired value for the boundary force. The numerical results for the PD and the robust adaptive controllers are presented in Figs. 6 through 11. Figures 6 and 7 demonstrate the step input responses to the second revolute joint of the MM3A®. It is observed from the stability and the performance of the PD and the RA controllers that both controllers are able to approach a desired value for θ_2. In addition, the error signal of the RA controller takes less time than the PD controller to settle.

From Figs. 8 and 9, it can be interpreted that the velocity tracking error for the step input response in the RA controller is bounded so that the tracking velocity error signal approaches zero.

https://doi.org/10.1017/S0263574714001441 Published online by Cambridge University Press

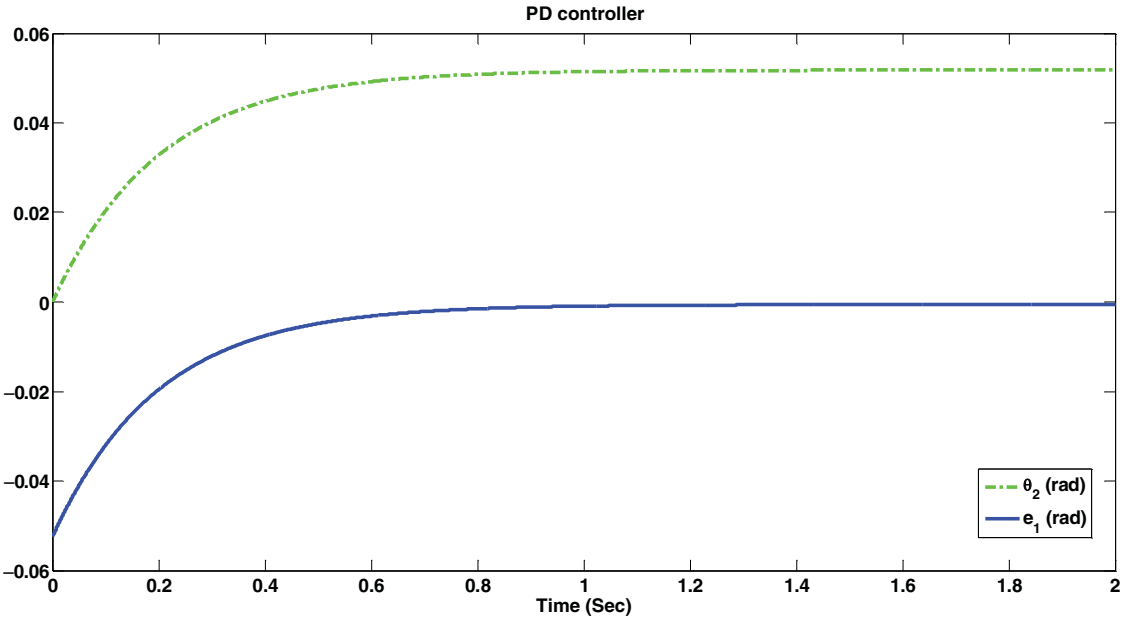


Fig. 6. SBFC—Time history of the step input response for θ_2 and its relevant error (PD controller).

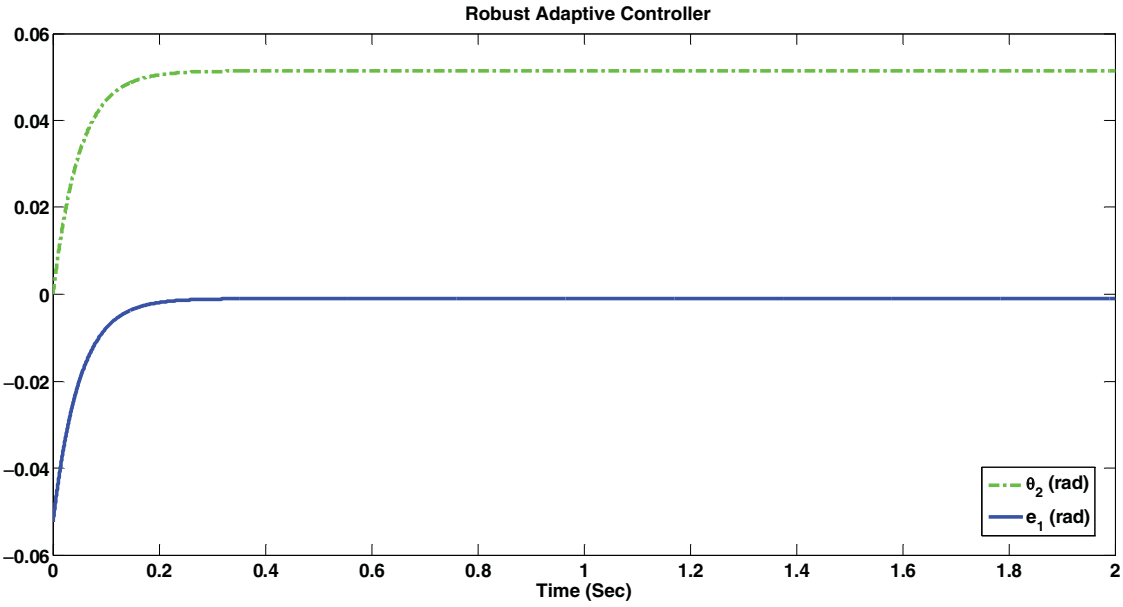


Fig. 7. SBFC—Time history of the step input response for θ_2 and its error,e_1 (RA controller).

In Figs. 10 and 11, the step input responses (e.g.,$f_{ID}^{D} = 5.5\ \mu$N) of the microcantilever's tip displacement mounted on the end effector of the MM3A® for both the PD and the RA controllers are illustrated. Since it is assumed that the boundary interaction force is a linear function of the tip displacement (Eq. (26)), the value of f_{ID} is also shown in the same graph. Looking closely at Figs. 10 and 11, it reveals that the response of the system by applying the PD and RA controller approaches the desired values within 0.2–0.4 (s).

The PD controller can be applied when the desired interaction force is assumed a constant value but may not be robust enough against disturbances and external noises influencing the system. However, in the case of DBFC, a dynamic trajectory for the interaction force is sought to be followed. For this end, a harmonic force is assumed to be the desired interaction force. Figures 12 and 13 show the

https://doi.org/10.1017/S0263574714001441 Published online by Cambridge University Press

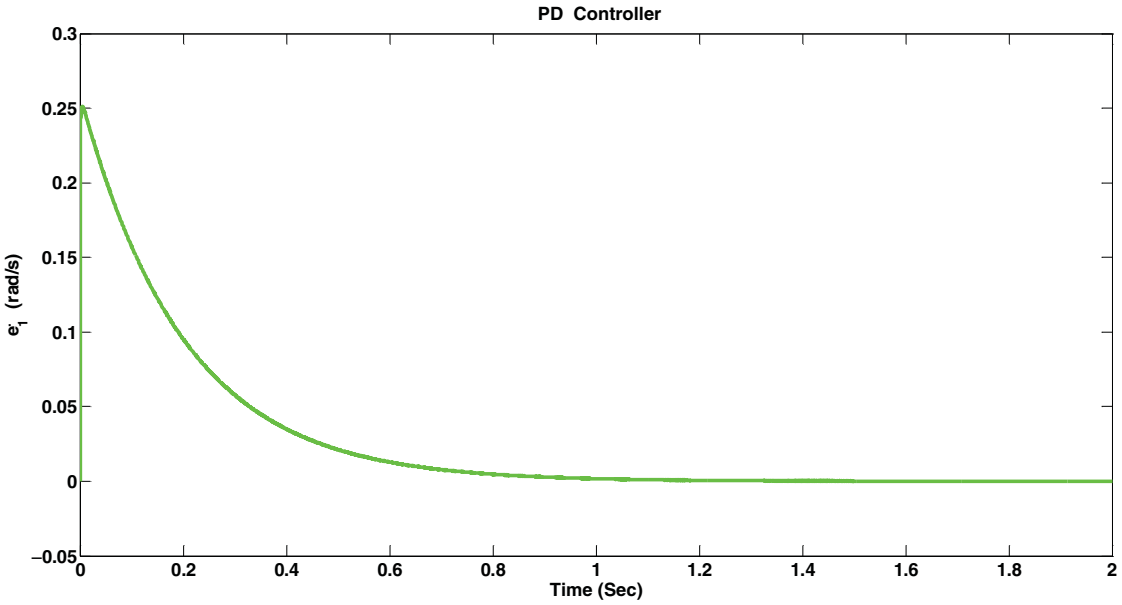


Fig. 8. SBFC—Time history of the step input response for $\dot{e}_1$ (PD controller).

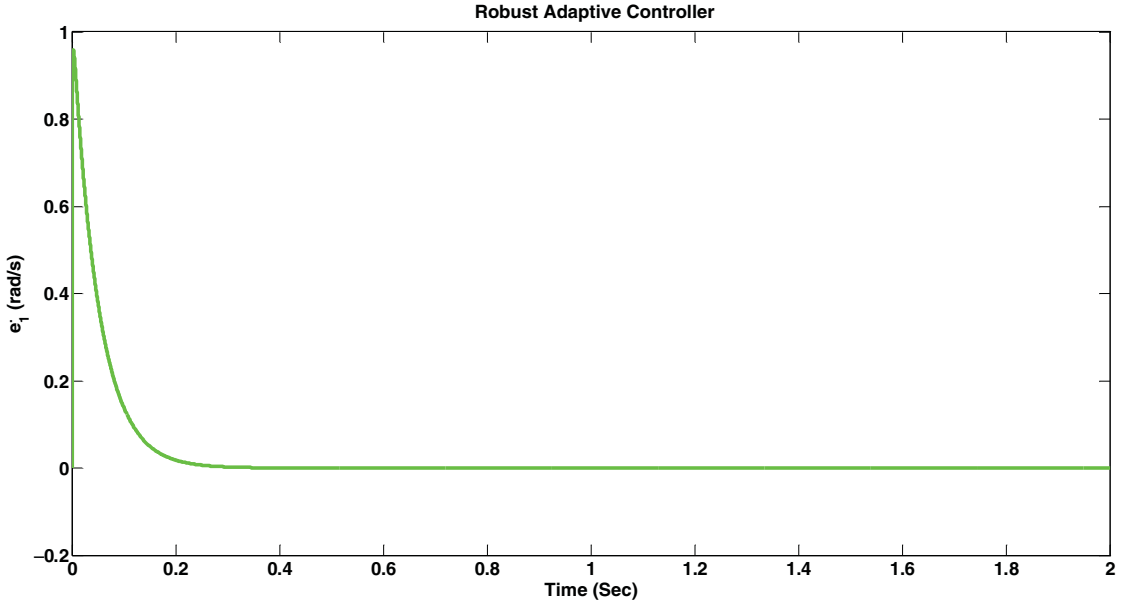


Fig. 9. SBFC—Time history of the step input response for $\dot{e}_1$ (RA controller).

actual and desired trajectories of the second revolute joint of the micromanipulator when the PD and the RA controllers are considered. Similarly, the trajectory errors are depicted in these figures. As expected, the RA controller behaves robustly supposing a dynamic trajectory for the second joint. On the other hand, estimated parameters (γ_0, γ_1, γ_2) converge asymptotically to the desired values as depicted in Fig. 14. However, the goal is to control the boundary interaction force when having a dynamic trajectory in such a way that the actual force is desired to follow that. Figure 15 demonstrates the performance and stability of the robust adaptive controller under various disturbances particularly unmodeled dynamics and noises and shows that it can asymptotically track the desired dynamic force ($[-25\ \mu\text{N} : 25\ \mu\text{N}]$) such that the error signal is always kept at a very small value. A white noise

https://doi.org/10.1017/S0263574714001441 Published online by Cambridge University Press

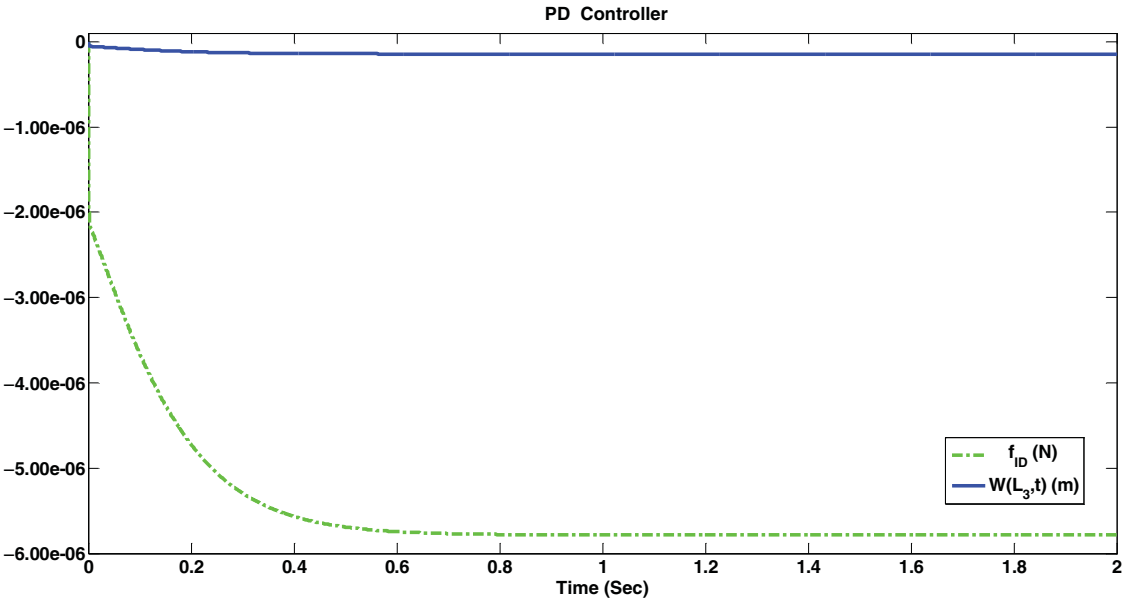


Fig. 10. SBFC—Time history of the step input response for f_{ID} and $w(L_3, t)$ (PD controller).

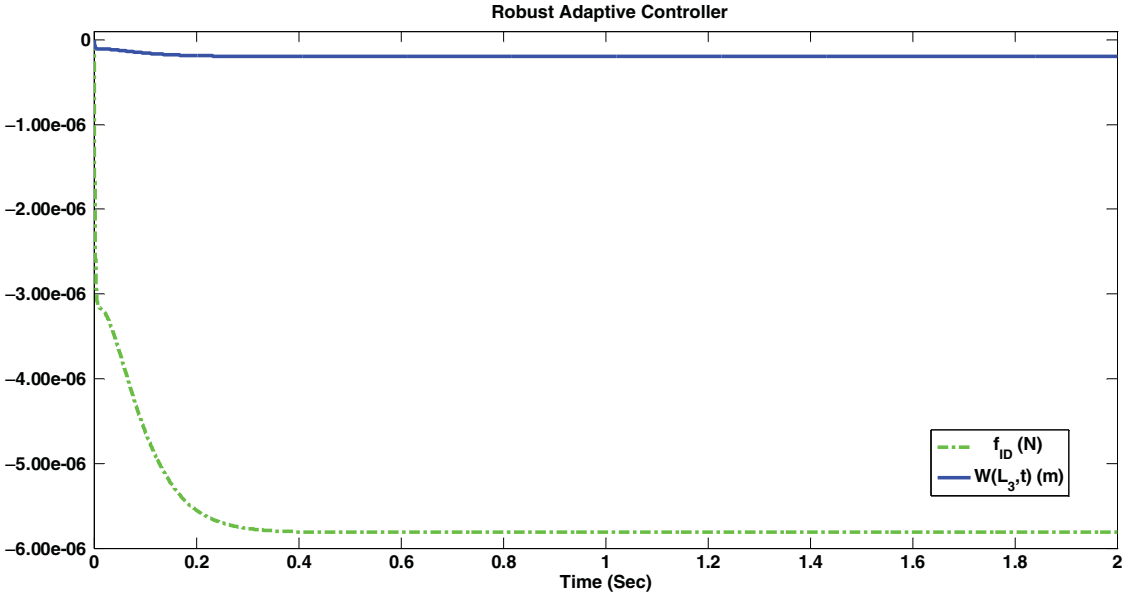


Fig. 11. SBFC—Time history of the step input response for f_{ID} and $w(L_3, t)$ (RA controller).

with zero mean value as an input disturbance is adopted for such a study and the results are shown in Figs. 12, 13, and 15.

5. Conclusions

In this paper, a comprehensive nonlinear model was considered for a 3-DOF revolute–revolute–prismatic micromanipulator accompanying a piezoresistive-based microcantilever as a force sensor. The task of the piezoresistive microcantilever is to sense the boundary interaction force by generating a voltage corresponding to a significant value of the interaction force. Along this line, the kinematics and dynamics modeling of a hybrid rigid-flexible micromanipulator with an integrated piezoresistive force sensor was presented. In the controller design scheme, two types of controllers were considered:

https://doi.org/10.1017/S0263574714001441 Published online by Cambridge University Press

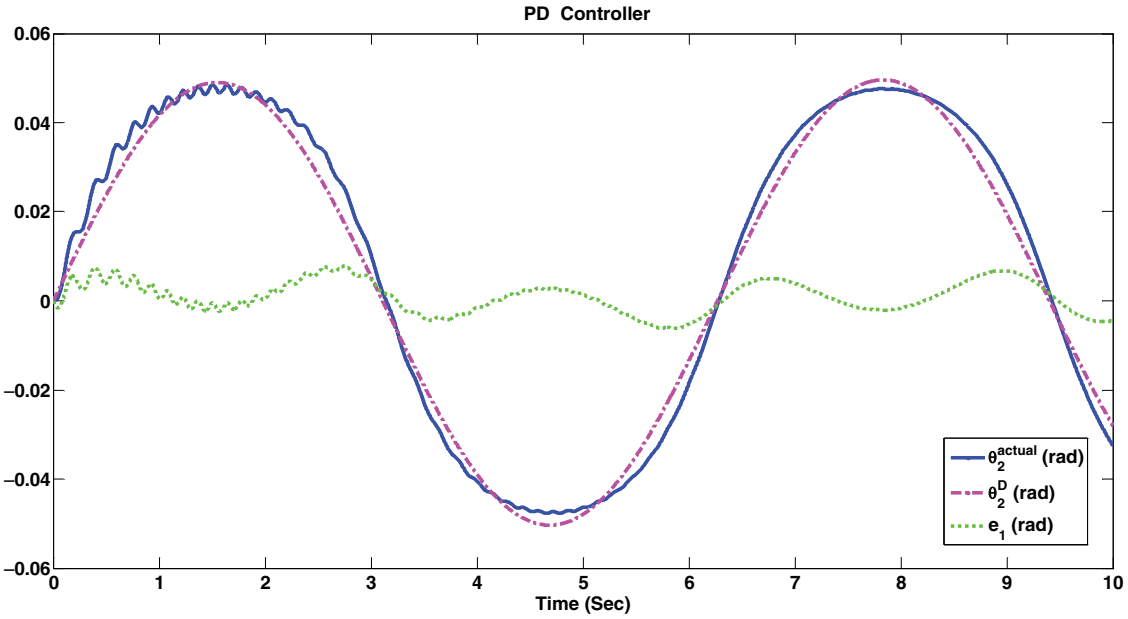


Fig. 12. DBFC—Time history of the actual and desired θ_2 and its error signal (PD controller).

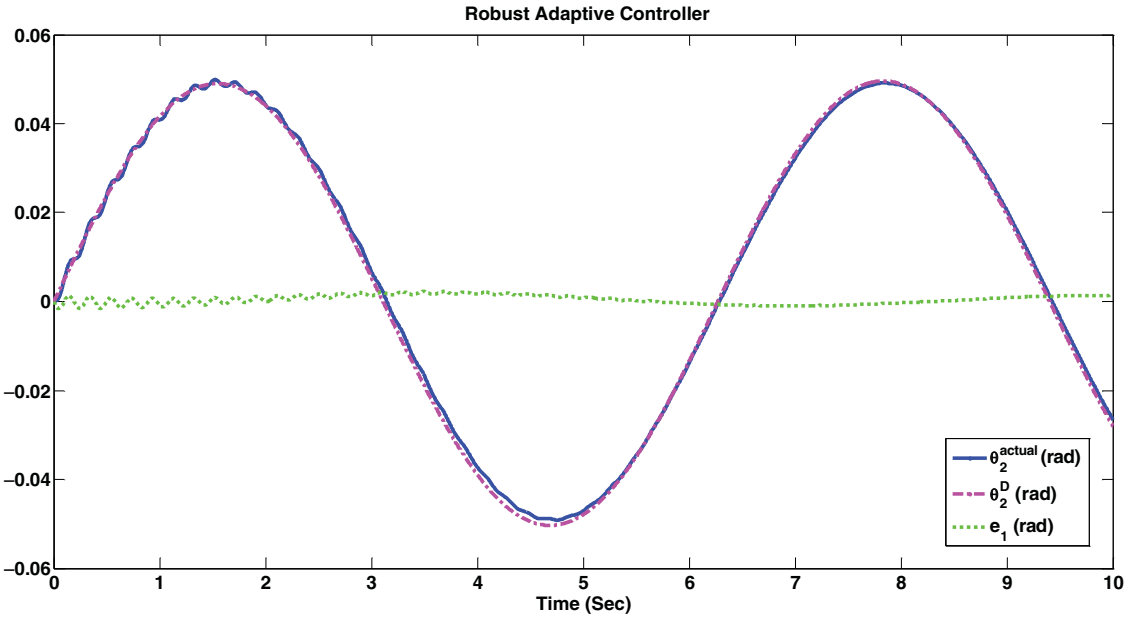


Fig. 13. DBFC—Time history of the actual and desired θ_2 and its error signal (RA controller).

a Lyapunov-based PD controller and a robust adaptive controller. For the step input control problem, the PD and the RA controllers provided the same performance but having a better performance against disturbances when utilizing the RA controller. On the other hand, for a dynamic force control problem, the RA controller was robust and suitable owing to possessing this capability to compensate for uncertainties and disturbances in the system and could be potentially implemented in real applications. Of those interesting applications of such system studied here is sensing and controlling the intermolecular forces,[28] micro/nanomanipulation, and cellular imaging of the biological samples. As the future work, it is interesting to assess more realistic interaction force models or implementing

https://doi.org/10.1017/S0263574714001441 Published online by Cambridge University Press

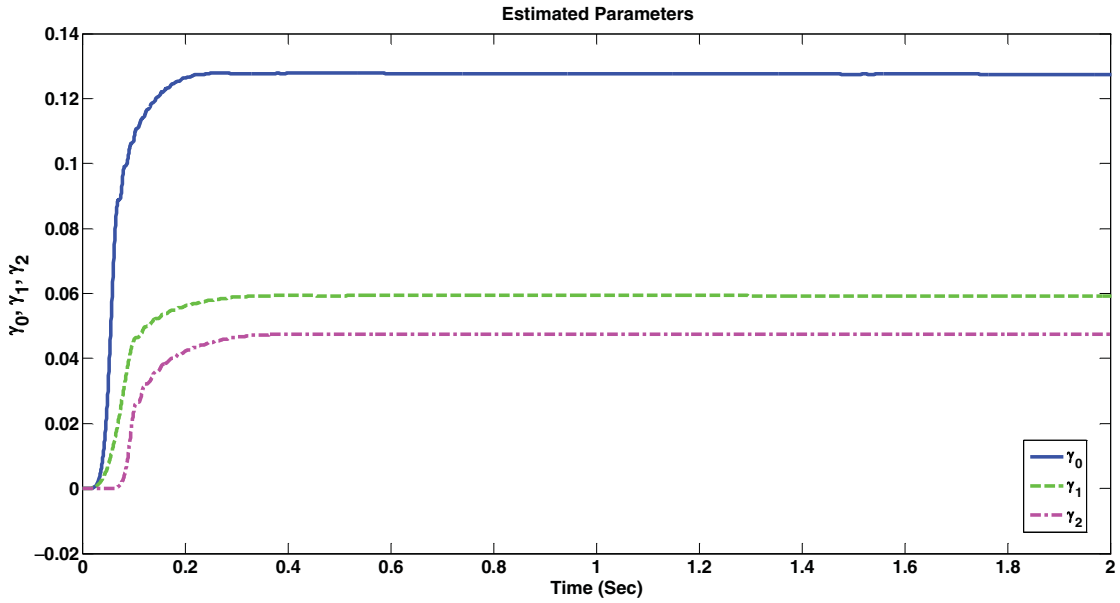


Fig. 14. Convergence of the estimated parameters γ_0, γ_1, γ_2 versus time.

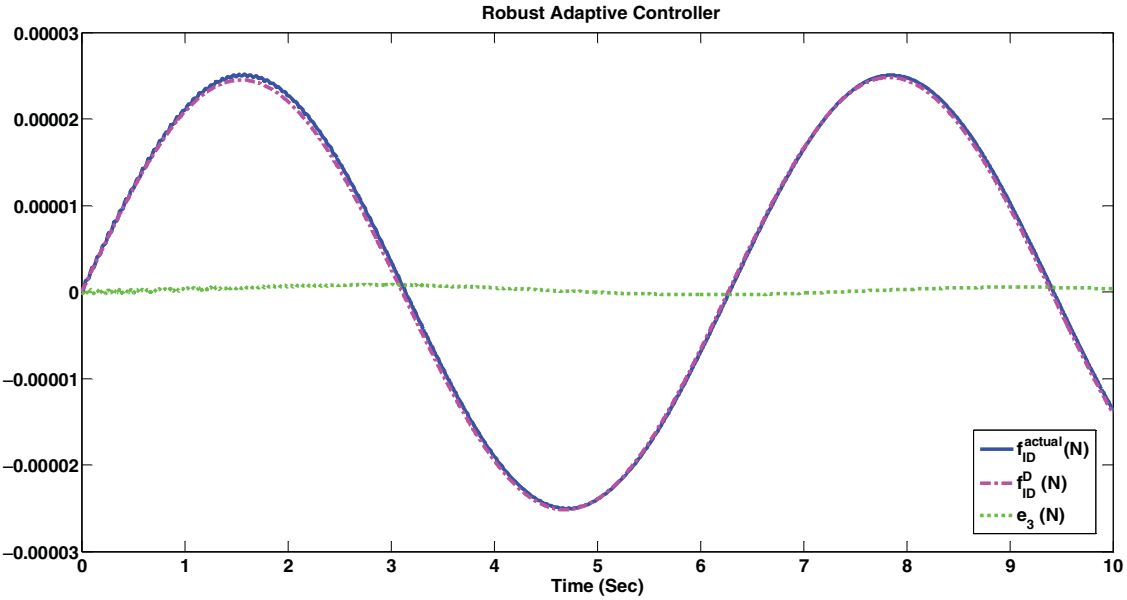


Fig. 15. DBFC—Time history of the actual and desired f_{ID} and its error signal (RA controller).

the control framework and the force feedback through the PMC force sensor presented here as a substitute of the vision feedback for automatically imaging of cellular/molecular surfaces.[29]

References

1. S. Kleindiek, MM3A® Micromanipulator, http://www.nanotechnik.com/mm3a-em.html
2. M. Flückiger, "Cell membrane mechanical modeling for microrobotic cell manipulation," Diploma Thesis WS2003/2004 (Zurich, Switzerland: IRIS Institute of Robotics and Intelligent Systems, ETHZ Swiss Federal Institute of Technology).
3. M. Guthold, M. R. Falvo, W. G. Matthews, S. Paulson, S. Washburn, D. Erie, R. Superfine, F. P. Brooks and R. M. Taylor, "Controlled Manipulation of Molecular Samples with the Nanomanipulator," *IEEE/ASME International Conference on Advanced Intelligent Mechatronics*, Atlanta, USA (1999) pp. 3–8.

https://doi.org/10.1017/S0263574714001441 Published online by Cambridge University Press

4. G. Li, N. Xi, M. Yu and W.K. Fung, "3D Nanomanipulation Using Atomic Force Microscopy", *IEEE International Conference on Robotics and Automation*, Taipei, Taiwan (2003) pp. 3642–3647.
5. Y. Yang, Z. Dong, M. Li and J. W. Li, "A Programmable AFM-Based Nanomanipulation Method Using Vibration-Mode Operation," *IEEE International Conference on Nano/Micro Engineered and Molecular Systems*, Sanya, China (2008) pp. 681–685.
6. I. Giouroudi, H. Hötzendorfer, D. Andrijasevic, M. Ferros and W. Brenner, "Design of Micrograpping System with Usual and Force Feedback for MEMS Application," *IEEE, the Institution of Engineering and Technology Seminar on MEMS Sensors and Actuators*, London, UK (2006) pp. 243–250.
7. R. Saeidpourazar and N. Jalili, "Towards fused vision and force robust feedback control of nanorobotic-based manipulation and grasping," *Mechatronics* **18**, 566–577 (2008).
8. S. Choura and A. S. Yigit, "Control of a two-link rigid-flexible manipulator with a moving payload mass," *J. Sound Vib.* **243**(5), 883–897 (2011).
9. A. A. Ata and H. Johar, "Dynamic simulation of task constrained of a rigid-flexible manipulator," *Int. J. Adv. Robot. Syst.* **1**(2), 61–66 (2004).
10. A. Fenili and J. M. Balthazar, "The rigid-flexible nonlinear robotic manipulator: Modeling and control," *Commun. Nonlinear Sci. Numer. Simul.* **16**, 2332–2341 (2011).
11. T. Chu Duc, J. F. Creemer and P. M. Sarro, "Piezoresistive cantilever beam for force sensing in two dimensions," *IEEE Sensors J.* **7**(1), 96–104 (2007).
12. S. J. Park, B. C. Petzold, M. B. Goodman and B. L. Pruitt, "Piezoresistive cantilever force-clamp system," *Rev. Sci. Instrum.* **82**, 043703 (10pp) (2011).
13. A. Behal, W. Dixon, D. M. Dawson and B. Xian, *Lyapunov-Based Control of Robotic Systems* (CRC Press, Boca Raton, FL, 2009).
14. F. R. Lewis, D. M. Dawson and C. T. Abdallah, *Robot Manipulator Control: Theory and Practice* (Marcel Dekker, Inc., New York, 2004).
15. W. E. Dixon, S. Nagarkatti, D. M. Dawson and A. Behal, *Nonlinear Control of Engineering Systems: A Lyapunov-Based Approach* (Birkhäuser Boston, New York, 2003).
16. M. S. de Queiroz, D. M. Dawson, S. P. Nagarkatti and F. Zhang, *Lyapunov-Based Control of Mechanical Systems* (Birkhäuser Boston, New York, 2000).
17. Z. Qu and D. M. Dawson, *Robust Tracking of Control of Robot Manipulators* (IEEE, 1996).
18. Kleindiek® CD, fms-em-v3.07 manual.
19. J. J. Craig, *Introduction to Robotics: Mechanics and Control*, 2nd ed. (Addison-Wiley, Reading, MA, 1989).
20. M. Dadfarnia, N. Jalili, B. Xian and D. M. Dawson, "A Lyapunov-based piezoelectric controller for flexible Cartesian robot manipulators," *ASME J. Dyn. Syst. Meas. Control* **126**(2), 347–358 (2004).
21. S. Eslami and N. Jalili, "A comprehensive modeling and vibration analysis of AFM microcantilevers subjected to nonlinear tip–sample interaction forces," *Ultramicroscopy* **117**, 31–45 (2012).
22. L. Tetard, A. Passian, S. Eslami, N. Jalili, R. H. Farahi and T. Thundat, "Virtual resonance and frequency difference generation by van der Waals interactions," *Phys. Rev. Lett.* **106**(18), 180801 (4pp) (2011).
23. Y. Zhou, B. Nelson and B. Vikramaditya, "Fusing Force and Vision Feedback for Micromanipulation," *Proceeding of the 1998 IEEE, International Conference on Robotics and Automation*, Leuven, Belgium (May, 1998).
24. A. Boisen, J. Thaysen, H. Jensenius and O. Hansen, "Environmental sensors based on micromachined cantilevers with integrated read-out," *Ultramicroscopy* **82**, 11–16(2000).
25. S. M. Yang and T. I. Yin, "Design and analysis of piezoresistive microcantilever for surface stress measurement in biological sensor," *Sensors Actuators* **120**, 734–744 (2007).
26. N. Jalili, *Piezoelectric-Based Vibration Control: From Macro to Micro/Nano Scale Systems*, ISBN: 1441900691, 1st ed. (Springer, NY, 2010).
27. J. Slotine and W. Li, *Applied Nonlinear Control* (Prentice Hall Co., Englewood Cliffs, NJ, 1991).
28. S. Eslami and N. Jalili, "Adaptive trajectory control of microcantilever's tip utilised in atomic force microscopy-based manipulation," *Int. J. Control* **84**(12), 1945–1955 (2011).
29. S. Eslami, R. Zareian and N. Jalili, "Integrated automated nanomanipulation and real-time cellular surface imaging for mechanical properties characterization," *Rev. Sci. Instrum.* **83**(10), 105002 (16pp). (Oct. 2012).

https://doi.org/10.1017/S0263574714001441 Published online by Cambridge University Press